AMERICAN JOURNAL OF PHYSIOLOGY
HEART AND CIRCULATORY PHYSIOLOGY

Am J Physiol Heart Circ Physiol 325: H113–H124, 2023.
First published June 2, 2023; doi:10.1152/ajpheart.00036.2023

RESEARCH ARTICLE

Vascular Biology and Microcirculation

Changes in transmural mass transport correlate with ascending thoracic aortic aneurysm diameter in a fibulin-4 E57K knockin mouse model

Christie L. Crandall,[1] Yufan Wu,[1] Keshav A. Kailash,[2] Mathew R. Bersi,[1] Carmen M. Halabi,[3] and Jessica E. Wagenseil[1]

[1]*Department of Mechanical Engineering and Materials Science, Washington University, St. Louis, Missouri, United States;* [2]*Department of Biomedical Engineering, Washington University, St. Louis, Missouri, United States; and* [3]*Pediatric Nephrology, Washington University School of Medicine, St. Louis, Missouri, United States*

Abstract

Thoracic aortic aneurysm is characterized by dilation of the aortic diameter by greater than 50%, which can lead to dissection or rupture. Common histopathology includes extracellular matrix remodeling that may affect transmural mass transport, defined as the movement of fluids and solutes across the wall. We measured in vitro ascending thoracic aorta mass transport in a mouse model with partial aneurysm phenotype penetration due to a mutation in the extracellular matrix protein fibulin-4 [*Fbln4*$^{E57K/E57K}$, referred to as MU-A (aneurysm) or MU-NA (no aneurysm)]. To push the aneurysm phenotype, we also included MU mice with reduced levels of lysyl oxidase [*Fbln4*$^{E57K/E57K}$;*Lox*$^{+/-}$, referred to as MU-XA (extreme aneurysm)] and compared all groups to wild-type (WT) littermates. The phenotype variation allows investigation of how aneurysm severity correlates with mass transport parameters and extracellular matrix organization. We found that MU-NA ascending thoracic aortae have similar hydraulic conductance (L_p) to WT, but 397% higher solute permeability (ω) for 4 kDa FITC-dextran. In contrast, MU-A and MU-XA ascending thoracic aortae have 44–68% lower L_p and similar ω to WT. The results suggest that ascending thoracic aortic aneurysm progression involves an initial increase in ω, followed by a decrease in L_p after the aneurysm has formed. All MU ascending thoracic aortae are longer and have increased elastic fiber fragmentation in the extracellular matrix. There is a negative correlation between diameter and L_p or ω in MU ascending thoracic aortae. Changes in mass transport due to elastic fiber fragmentation could contribute to aneurysm progression or be leveraged for treatment.

NEW & NOTEWORTHY Transmural mass transport is quantified in the ascending thoracic aorta of mice with a mutation in fibulin-4 that is associated with thoracic aortic aneurysms. Fluid and solute transport depend on aneurysm severity, correlate with elastic fiber fragmentation, and may be affected by proteoglycan deposition. Transport properties of the ascending thoracic aorta are provided and can be used in computational models. The changes in mass transport may contribute to aneurysm progression or be leveraged for aneurysm treatment.

aneurysm; ascending thoracic aortic aneurysm; convection; diffusion; extracellular matrix; transport

INTRODUCTION

Thoracic aortic aneurysms (TAAs) are characterized by a focal dilation causing at least a 50% increase in aortic diameter (1). Described as "silent killers," TAAs can go undiagnosed until rupture occurs, which is often fatal (2). More than 20% of TAAs are linked to genetic mutations (3). These mutations can be associated with genes involved in the assembly or cross linking of elastic fibers in the aortic extracellular matrix. Elastic fibers are concentrated in the medial (middle) layer of elastic arteries, such as the aorta, where they are arranged in dense, fibrous sheets called elastic laminae. The elastic laminae are essential for mechanical recoil during the cardiac cycle. Beyond their mechanical function, the elastic laminae also form a physical barrier between layers of smooth muscle cells within the aortic media and have been hypothesized to provide immune privilege to this region (4) and modulate mass transport (5). TAA histopathology is associated with increased elastic fiber fragmentation or disorganization (6) and increased proteoglycan content (7), but how these changes in extracellular matrix organization are related to TAA progression is not fully understood. We are interested in the role that changes in transmural mass transport, due to changes in the aortic extracellular matrix, may play in TAA pathology.

Correspondence: J. E. Wagenseil (jessica.wagenseil@wustl.edu).
Submitted 23 January 2023 / Revised 22 May 2023 / Accepted 25 May 2023

0363-6135/23 Copyright © 2023 the American Physiological Society.

Downloaded from journals.physiology.org/journal/ajpheart at Washington Univ (128.252.014.100) on June 29, 2023.

The endothelial cell layer at the arterial lumen is the initial and most prominent barrier to transmural mass transport; however, TAA is often associated with endothelial dysfunction and impaired barrier capabilities (8). Hence, mass transport through the medial and adventitial (outer) layers of the aortic wall may be especially important in TAA. Fenestrations or holes in the elastic laminae, particularly in the inner elastic lamina (IEL), are thought to facilitate transmural mass transport (9). Mouse models of TAA caused by mutations in elastic fiber-associated genes have increased IEL fenestration number and size (10). Fragmented elastic laminae, due to genetic mutations or enzymatic degradation, increase fluid and solute transport in mouse carotid arteries (11); however, carotid arteries do not typically develop aneurysms. Mass transport has been studied in the ascending thoracic aorta (ATA) of mice with a heterozygous missense mutation in lysyl oxidase ($Lox^{M292R/+}$), an enzyme critical to cross linking of collagen and elastic fibers that is associated with TAA in humans (12). $Lox^{M292R/+}$ mice have a greater number of elastic fiber breaks and increased fluid and solute mass transport in the presence of an osmotic pressure gradient, yet do not have differences in IEL fenestration number or size (13) and do not develop TAA without an additional hemodynamic stressor, such as increased blood pressure (14).

Here, we use a mouse model with a homozygous knockin mutation of fibulin-4 ($Fbln4^{E57K/E57K}$), which recapitulates a genetic mutation associated with TAA in humans (15). Fibulin-4 is essential for proper elastic fiber assembly (16) and interacts with lysyl oxidase to assist in collagen and elastic fiber cross linking (17). $Fbln4^{E57K/E57K}$ mice develop ATA aneurysms with ~50% penetrance and have hypertension in addition to elongated, tortuous arteries (18). We found that breeding $Fbln4^{E57K/E57K}$ mice with lysyl oxidase haploinsufficient mice ($Lox^{+/-}$) (19) induces ATA aneurysms with 100% penetrance. In the current study, we measured mass transport properties in the ATA of $Fbln4^{E57K/E57K}Lox^{+/+}$, $Fbln4^{E57K/E57K}Lox^{+/-}$, and $Fbln4^{+/+}Lox^{+/+}$ (wild type, WT) mice. We hypothesized that extracellular matrix defects due to the genetic mutations primarily affecting elastic fibers in these TAA models would alter transmural mass transport and that changes in mass transport may correlate with aneurysm severity. In vitro fluid and solute flux were measured in both solute-absent and solute-present conditions with the ATA axially stretched and pressurized to physiological values. Material parameters of hydraulic conductance and solute permeability were calculated using one-dimensional (1-D) advection-diffusion equations. To quantify extracellular matrix organization, we stained and imaged ATA cross sections and en face preparations using light and/or electron microscopy.

METHODS

Mice

Mice with a homozygous missense mutation in fibulin-4 ($Fbln4^{E57K/E57K}$) were used as a genetic TAA model. $Fbln4^{E57K/E57K}$ mice have cutis laxa, or loose skin, and elongated ATAs with 50% penetrance of the aneurysm phenotype (15). To increase ATA aneurysm incidence and/or severity, we bred $Fbln4^{E57K/E57K}$ mice to lysyl oxidase haploinsufficient mice ($Lox^{+/-}$) (19). $Lox^{-/-}$ mice die at birth, and $Lox^{+/-}$ mice have reduced lysyl oxidase expression, but no obvious cardiovascular phenotype. Because of the interactions between fibulin-4 and lysyl oxidase during elastic fiber assembly, we hypothesized that the effect of the fibulin-4 mutation on ATA aneurysms would be exacerbated in an environment of reduced lysyl oxidase. Indeed, $Fbln4^{E57K/E57K}$;$Lox^{+/-}$ mice (termed MU-XA for mutant, extreme aneurysm) had 100% ATA aneurysm penetrance. For the regular fibulin-4 mutant mice ($Fbln4^{E57K/E57K}Lox^{+/+}$), we divided them into two groups (termed MU-A for mutant, aneurysm and MU-NA for mutant, no aneurysm) depending on whether or not they met the clinical criteria for an aneurysm of 50% larger ATA diameter than wild-type control ($Fbln4^{+/+}Lox^{+/+}$, termed WT). WT, MU-NA, and MU-A groups had an n = 14, 11, and 9, respectively, and were approximately half male and half female. Because of poor survival rates, only n = 8 were included for the MU-XA group, with five male and three female mice. Males and females were combined for all analyses as we were not powered to investigate sex differences, and previous studies do not suggest significant sex differences in aortic mass transport (13). Mice were euthanized between 3 and 4 mo of age by carbon dioxide inhalation. All animal procedures were approved by Washington University's Institutional Animal Care and Use Committee. ATAs were dissected, isolating the region from the base of the heart to the innominate artery, and kept at 4°C in phosphate-buffered saline (PBS) for up to 3 days before experimentation.

Transport Measurements

A fluid column of PBS was attached to the inlet of a pressure myograph (110P, Danish Myo Technology) and adjusted to pressurize the entire fluid system at 100 mmHg for 12 + h before the experiment (Fig. 1*A*). ATAs were mounted on cannulae using 7-0 sutures and placed into a bath of PBS at 37°C. An air bubble was passed through the lumen to disrupt the endothelial cell layer. The ATA was stretched to an approximate in vivo axial stretch ratio of 1.1× (20) and exposed to the 100-mmHg static pressure column. An image of the loaded ATA was taken using a digital camera (Fig. 1*B*). A bubble was introduced into the lead tubing and its displacement was recorded over time to measure fluid flow velocity (Fig. 1*A*). After 30 min, the intraluminal PBS was replaced with a solution of 5 mg/mL of 4-kDa FITC-dextran (Sigma-Aldrich) in PBS. A new bubble was introduced into the lead tubing, and the system was equilibrated at 100 mmHg for 30 min. The outer surface of the ATA was then rinsed, the bath was refilled with 7 mL of fresh PBS, and both the bubble movement and concentration of the bath were recorded for 70 min. Fluid flux was calculated using measurements of the change in displacement over time (dx/dt) from the bubble tracking for both solute-absent (J_v) and solute-present (J_{vs}) experiments. Solute flux (J_s) was calculated from the change in concentration of the bath over time (dc/dt) (11). Both values were normalized by ATA outer surface area using a membrane approximation. Outer surface area was calculated from two-dimensional (2-D) images of mounted and loaded ATAs using Matlab software (Mathworks). The right and left sides of each ATA were identified in the images and rotated

Downloaded from journals.physiology.org/journal/ajpheart at Washington Univ (128.252.014.100) on June 29, 2023.

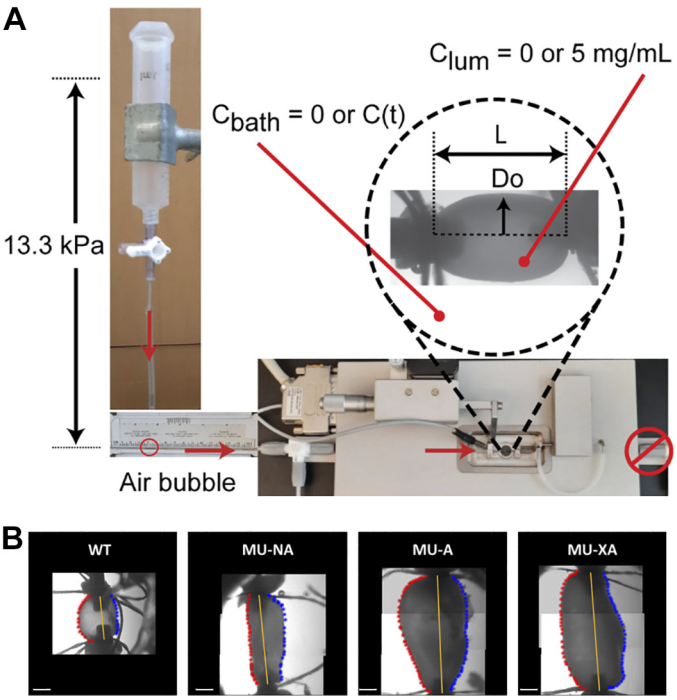

Figure 1. Experimental set-up. *A*: ascending thoracic aorta (ATA) was mounted in a pressure myograph and secured with 7-0 sutures. It was stretched to 1.1 axial stretch ratio and pressurized to 100 mmHg by a static fluid pressure column of phosphate-buffered saline (PBS). Axial length (L) and outer diameter (D_o) were recorded. An air bubble was inserted into the tubing to track fluid flux through the wall. Both solute-absent (C_{lum} = C_{bath} = 0) and solute-present (C_{lum} = 5 mg/mL 4-kDa FITC-dextran and C_{bath} = measured C_t) experiments were performed for each ATA. *B*: representative images of mounted ATAs from wild-type (WT) and mutant (MU; *Fbln4*$^{E57K/E57K}$) groups at 1.1 axial stretch and 100 mmHg. The longitudinal axis is traced with a yellow line, and left/right edges are shown in red/blue dots. Scale bars = 0.5 mm. MU-A, *Fbln4*$^{E57K/E57K}$, aneurysm; MU-NA, *Fbln4*$^{E57K/E57K}$, nonaneurysm; MU-XA, *Fbln4*$^{E57K/E57K}$;*Lox*$^{+/-}$, extreme aneurysm.

about the longitudinal axis to approximate the outer surface area (Fig. 1*B*).

Transport Theory

We used a 1-D advection-diffusion mass transport equation to describe the transmural fluid flux in response to a pressure (ΔP) and solute gradient (Δc). Transmural flow was assumed to only be in the radial direction. To calculate hydraulic conductance (L_p), a material parameter describing fluid transport through a semipermeable membrane, we used (21)

$$L_p = \frac{J_v}{\Delta P - \sigma RT\Delta c}, \quad (1)$$

where σ is a reflection coefficient, R is the gas constant, and T is the absolute temperature. When solute was absent (Δc = 0), L_p in *Eq. 1* was calculated from our measured experimental quantities (ΔP, J_v). When solute was present ($\Delta c \neq 0$), L_p in *Eq. 1* was calculated from our measured experimental quantities (ΔP, J_{vs}, Δc) and an assumed value for σ. When solute was present, we also calculated the solute permeability (ω), a material parameter describing solute transport through a semipermeable membrane, from the solute-present fluid flux (J_{vs}) and solute flux (J_s) due to diffusive movement and an average solute concentration (c_s) moved by advection,

$$\omega = \frac{J_s - (1-\sigma')c_s J_{vs}}{RT\Delta c}, \quad (2)$$

where σ' is another reflection coefficient. The reflection coefficients must lie between 1 (impermeable to solute) and 0 (equally permeable to solvent and solute) (22). Values of $\sigma <$ 0.99 produced $\omega < 0$ for our experimental measurements, yet $\sigma < 1$ must be true for solute transport. Hence, we assumed that $\sigma = \sigma' = 0.99$ (23) and calculated solute-absent (L_p) and solute-present (L_{ps}) hydraulic conductance and solute permeability (ω) for each ATA.

Electron Microscopy Imaging

Additional WT, MU-NA, MU-A, and MU-XA mice (1–2/group) were euthanized, and ATAs were dissected after pressure fixation, as previously described (18). Briefly, ATAs were fixed in 10% neutral-buffered formalin (Sigma-Aldrich) for 1 wk and then in 2.5% glutaraldehyde (EMS) for 2–3 wk at 4°C. Samples were then washed in PBS, postfixed with 1.25% osmium tetroxide (EMS), and stained sequentially with 2% tannic acid (Sigma-Aldrich) and 6% uranyl acetate (EMS). Samples were washed again and dehydrated in a graded series of ethanol. Samples were then infiltrated in a graded series of resin and propylene oxide (PolySciences) before embedding in fresh resin. Blocks were sectioned at 60 nm thickness, collected on formvar-coated grids, poststained with 6% uranyl acetate, and imaged on a JEOL 1400 electron microscope with an AMT XR111 digital camera at the Washington University Center for Cellular Imaging.

Light Microscopy Imaging

Postexperimentation, ATAs were fixed in 4% paraformaldehyde (Sigma-Aldrich) while pressurized at 100 mmHg for 12–20 h. ATAs were then sequentially dehydrated and stored in 70% ethanol before use. To prepare for multiphoton imaging, ATAs were rehydrated and n = 3/group were halved where the inferior half was sliced along the longitudinal axis and butterflied open for en face imaging. The superior halves and an additional n = 2–3/group of ATAs were flash frozen in optimal cutting temperature (OCT) compound for cryosectioning. Cross sections (10 μm) were placed onto frosted-plus microscope slides and stored at −20°C before multiphoton imaging.

En face samples and cross sections were imaged using a Leica Sp-8 DIVE multiphoton microscope with a ×40 objective. Collagen and elastin were excited at 880 nm and imaged using second-harmonic generation (emission, 420–460 nm) and autofluorescence (emission, 495–540 nm), respectively. Quantification of elastic-laminae fragmentation was performed on the elastin images. For cross-sectional images, a 144 × 192-μm region was isolated in ImageJ software (NIH), and a threshold was applied to create a binary mask. The skeletonize function was then used to quantify image features (24). Junctions are defined as any pixel that has greater than two neighboring pixels of the same color, end points are any pixels with less than two neighbors, and slabs are the rest of the connected pixels. *Z*-stacks were taken of the en

Downloaded from journals.physiology.org/journal/ajpheart at Washington Univ (128.252.014.100) on June 29, 2023.

face images to capture the entire IEL. Regions of the IEL were isolated in a maximum z-projection and a 192 × 192-μm in-plane region was isolated for feature analysis. A binary mask was created by thresholding and then uploaded into Matlab software to calculate the number of holes and the ratio of white (hole) to black (IEL) area.

Additional fixed ATA samples (n = 3/group) were processed for histological staining. Samples were embedded in paraffin, 5-μm cross sections were cut, and stained with Movat's pentachrome that highlights elastic fibers (black), collagen (yellow), cell cytoplasm (red), and proteoglycans (blue). Stained sections were imaged on an Olympus DP80 microscope using a ×40 objective.

Statistical Analysis

All statistical analyses were conducted using GraphPad Prism. Two and one outliers were removed using the ROUT test for the solute-absent and solute-present experimental data, respectively. The four experimental groups were compared using an ordinary one-way ANOVA. If significant ($P < 0.05$), Sidak's post hoc test was used for multiple comparison testing. Data are presented with means and standard deviations. Correlations were analyzed using the Pearson correlation coefficient, r. Correlation strength (r), goodness of fit (R^2), and statistical significance (P) are reported.

RESULTS

Geometry and Aneurysm Characterization

Images of the loaded (1.1× axial stretch and 100 mmHg internal pressure) ATAs (Fig. 1*B*) were analyzed to determine maximum outer diameter, longitudinal axis length (suture-to-suture distance), and outer surface area (Fig. 2). MU-NA and MU-A samples were separated by comparing each ATA outer diameter to the average WT outer diameter (1,308 μm) and using the clinical criteria that an aneurysm is >50% diameter dilation. When compared with WT, MU-NA ATAs have similar outer diameters, whereas MU-A have 87% larger outer diameters and MU-XA have 93% larger outer diameters (Fig. 2*A*). All MU ATAs are 100–160% longer than WT (Fig. 2*B*). Outer surface area increases 129, 329, and 378%, respectively, for MU-NA, MU-A, and MU-XA ATAs, compared with WT (Fig. 2*C*). No significant differences in geometry are found comparing MU-A to MU-XA ATAs. These data illustrate the geometric variations in aneurysm phenotype across groups.

Mass Transport

Bubble displacement was recorded for 30 min and used to calculate the fluid flux. This was done in both solute-absent (Fig. 3, *A* and *B*) and solute-present (Fig. 3, *C* and *D*) conditions. Bubble displacement trends higher in MU ATAs but fluid flux, which is normalized by the outer surface area, is lower. MU-A and MU-XA ATAs have 59–67% lower fluid flux with solute absent and 44–68% lower fluid flux with solute present, compared with WT. The change in bath concentration over 70 min was used to calculate the solute flux (Fig. 3, *E* and *F*). The change in bath concentration is highest in the MU-NA and lowest in the WT ATAs. This pattern remains for the solute flux, which is normalized by outer surface area. MU-NA values of solute flux are 394, 109, and 436% higher than WT, MU-A, and MU-XA ATAs, respectively. There are no significant differences in solute flux for the MU-A and MU-XA ATAs compared with WT.

Hydraulic conductance was calculated from *Eq. 1*. Like the fluid flux, MU-A and MU-XA ATAs have 59–67% lower hydraulic conductance with solute absent and 44–68% lower hydraulic conductance with solute present, compared with WT (Fig. 4, *A* and *B*). Solute permeability was calculated from *Eq. 2*. Like the solute flux, MU-NA solute permeability is 397, 109, and 436% higher than WT, MU-A, and MU-XA ATAs, respectively. These data show changes in fluid and solute transport properties that depend on aneurysm phenotype.

Extracellular Matrix Organization

Electron microscopy images of the ATA wall for the four groups are shown in Fig. 5 to demonstrate the ultrastructural effects of the genetic mutations. Most notably, elastic laminae in MU ATAs are fragmented and discontinuous compared with WT (Fig. 5*A*). MU ATAs have a very thin, sparse IEL near the lumen (Fig. 5*B*). Although not quantitative, the

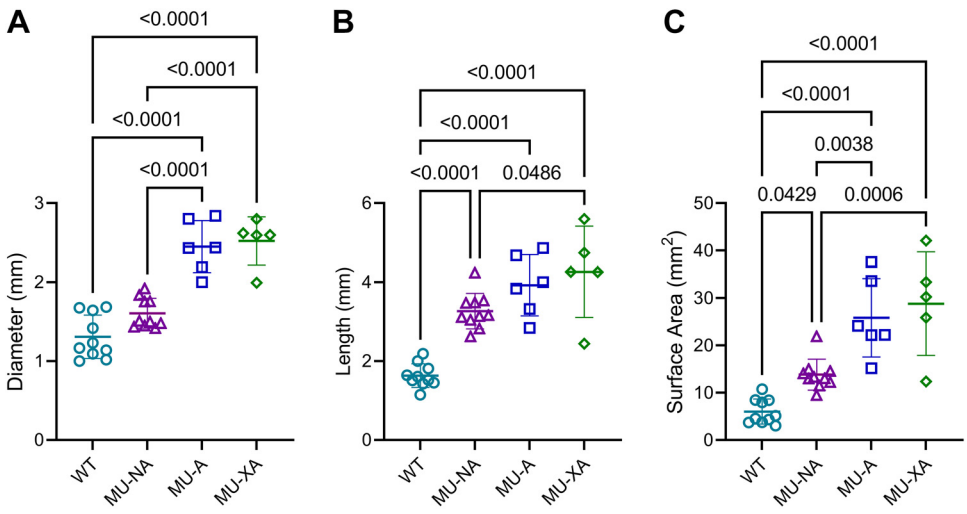

Figure 2. Maximum outer diameter (*A*), axial length (*B*), and outer surface area (*C*) of ascending thoracic aortas (ATAs) were measured from pictures taken of mounted ATAs at 1.1× axial stretch ratio and pressurized to 100 mmHg. Significant *P* values are shown for a one-way ANOVA with Sidak's multiple comparisons. n = 5–10/group. MU-A, *Fbln4*$^{E57K/E57K}$, aneurysm; MU-NA, *Fbln4*$^{E57K/E57K}$, nonaneurysm; MU-XA, *Fbln4*$^{E57K/E57K}$;*Lox*$^{+/-}$, extreme aneurysm; WT, wild type.

Downloaded from journals.physiology.org/journal/ajpheart at Washington Univ (128.252.014.100) on June 29, 2023.

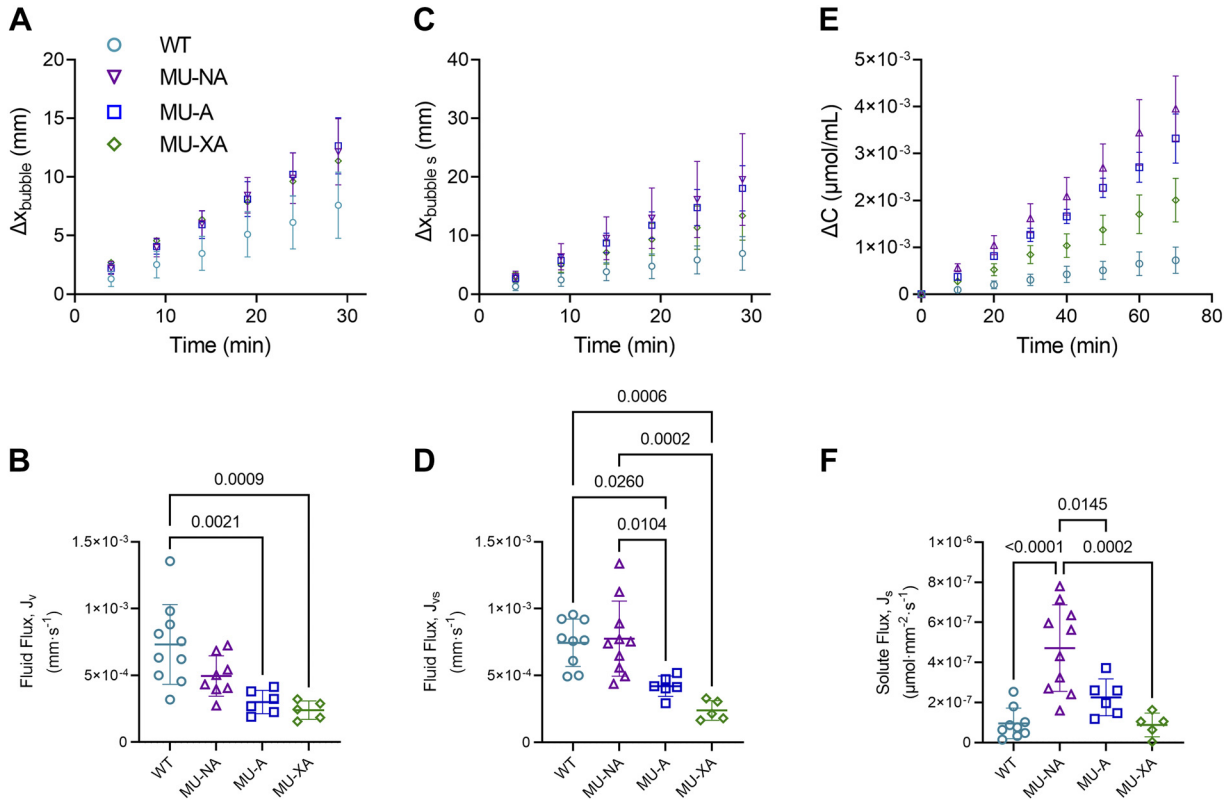

Figure 3. Plots of bubble displacement vs. time and the calculated fluid flux for solute-absent (*A* and *B*) and solute-present (*C* and *D*) conditions. Plots of the change in concentration of the surrounding bath vs. time (*E*) and the calculated solute flux (*F*) of the 4-kDa FITC-dextran solute. All three measurements were normalized to begin at 0. Significant *P* values are shown for a one-way ANOVA with Sidak's multiple comparisons. *n* = 5–10/group. MU-A, *Fbln4*$^{E57K/E57K}$, aneurysm; MU-NA, *Fbln4*$^{E57K/E57K}$, nonaneurysm; MU-XA, *Fbln4*$^{E57K/E57K}$;*Lox*$^{+/-}$, extreme aneurysm; WT, wild type.

electron microscopy images suggest increased elastic-laminae fragmentation and thinning in MU-XA ATAs compared with MU-A and MU-NA ATAs.

As electron microscopy requires extensive tissue processing and only shows a small segment of the ATA wall, we used multiphoton microscopy to further investigate structural changes in the extracellular matrix, with a focus on elastic-laminae organization. Representative cross-sectional images of elastin and collagen are shown for each experimental group (Fig. 6*A*). The elastic laminae in the MU ATAs are less distinct, and elastin layers extend into the adventitia, interspersing with the collagen. The elastin images were quantified, and structural

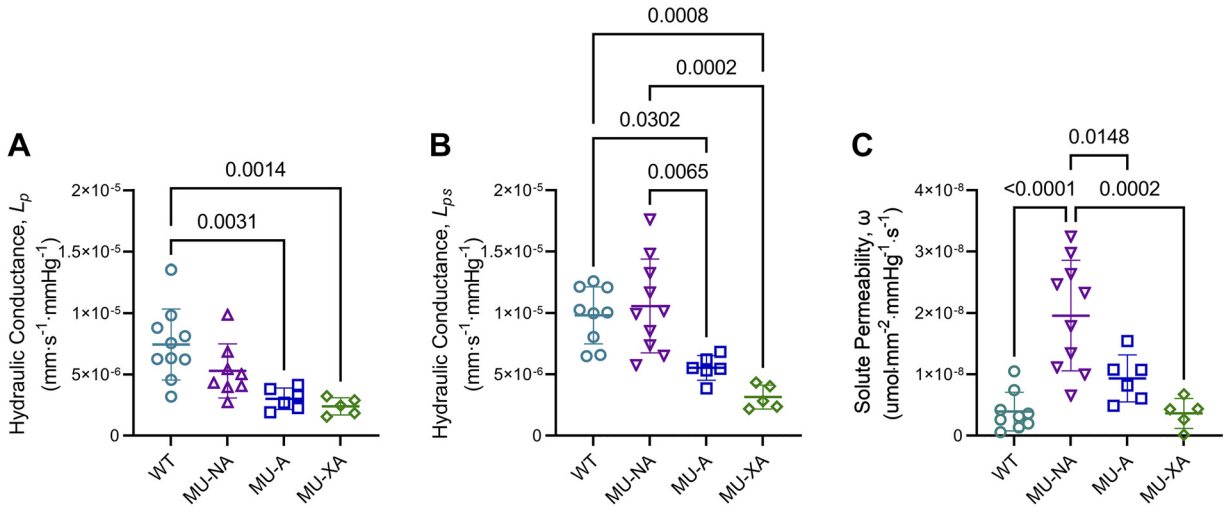

Figure 4. Calculated values of solute-absent hydraulic conductance (*A*), solute-present hydraulic conductance (*B*), and solute permeability (*C*) from one-dimensional (1-D) advection diffusion equation. Significant *P* values are shown for a one-way ANOVA with Sidak's multiple comparisons. *n* = 5–10/group. MU-A, *Fbln4*$^{E57K/E57K}$, aneurysm; MU-NA, *Fbln4*$^{E57K/E57K}$, nonaneurysm; MU-XA, *Fbln4*$^{E57K/E57K}$;*Lox*$^{+/-}$, extreme aneurysm; WT, wild type.

Downloaded from journals.physiology.org/journal/ajpheart at Washington Univ (128.252.014.100) on June 29, 2023.

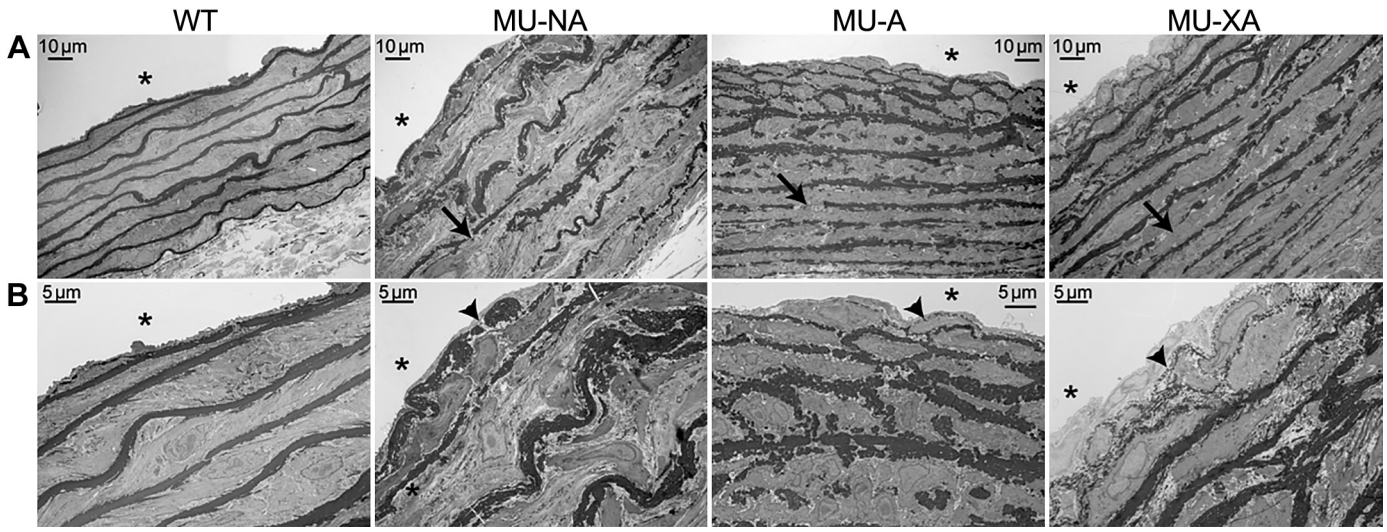

Figure 5. Representative electron microscopy images of ascending thoracic aorta (ATA) cross sections from the four experimental groups. The lumen is marked (*), and elastic laminae are stained black/dark gray. Arrows in *A* indicate fragmented elastic laminae. Arrowheads in *B* indicate locations of fragmented and/or thin internal elastic lamina (IEL). Images are representative of n = 1–2/group. MU-A, *Fbln4*$^{E57K/E57K}$, aneurysm; MU-NA, *Fbln4*$^{E57K/E57K}$, nonaneurysm; MU-XA, *Fbln4*$^{E57K/E57K}$;*Lox*$^{+/-}$, extreme aneurysm; WT, wild type.

comparisons were made across groups. MU-XA has 54% thicker walls compared with WT (Fig. 6*C*). Junctions (Fig. 6*D*), slab size (Fig. 6*E*), and end points (Fig. 6*F*) of the elastic laminae were identified using the skeletonize function in ImageJ (Fig. 6*B*) and were normalized to the wall area of each image. Junctions are 164% higher only in MU-NA ATA compared with WT; however, MU-A and MU-XA ATAs show similar trends to MU-NA. Average slab size is no different between groups but tends to be higher in the MU-ATAs. End points are more frequent in MU-NA, MU-A, and MU-XA ATAs compared

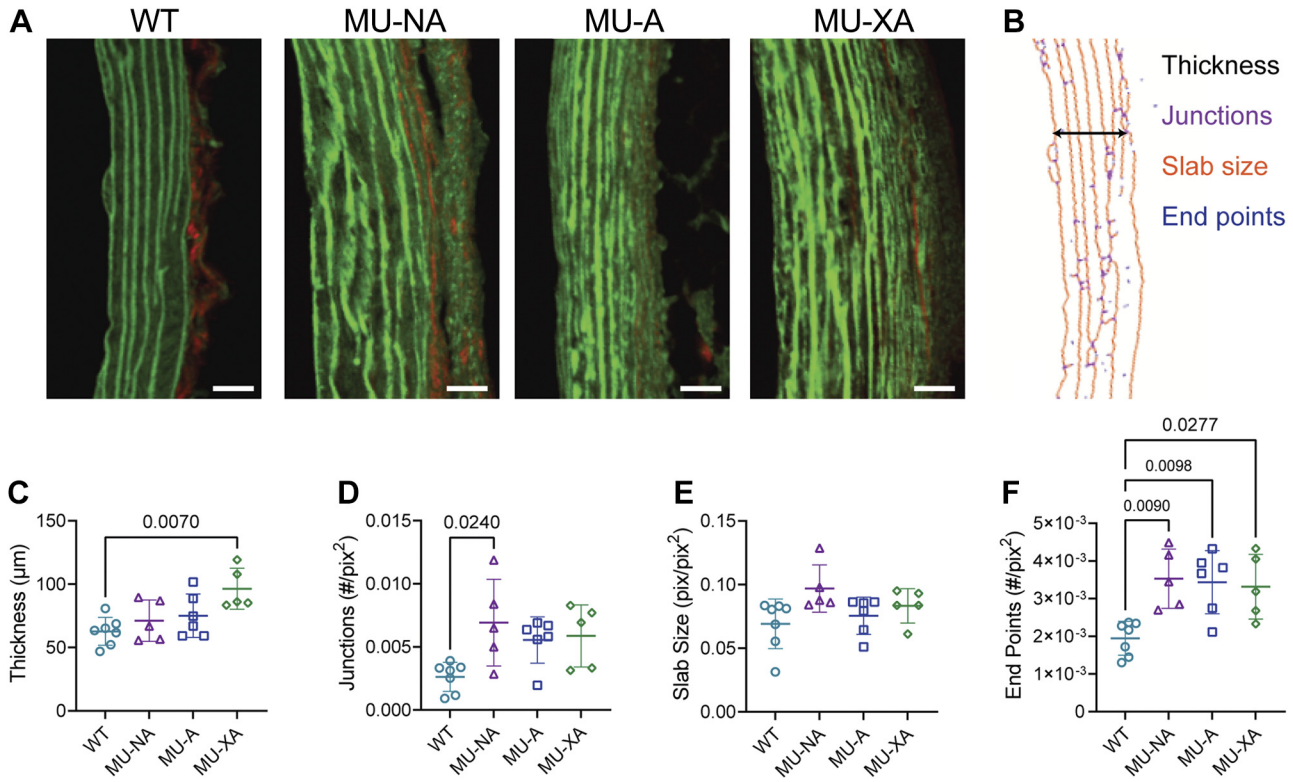

Figure 6. Representative cross-sectional multiphoton images of the ascending thoracic aorta (ATA) from the four experimental groups (*A*). Elastin is green, collagen is red, and scale bars = 20 μm. The lumen is on the *left*. Elastin images were skeletonized [*B* shows wild type (WT) example] to quantify elastic-laminae structure. Thickness of the ATA wall was quantified, as well as the elastic-laminae junctions, average slab size, and end points (*C*–*F*). Significant P values are shown for a one-way ANOVA with Sidak's multiple comparisons. n = 5–7/group. MU-A, *Fbln4*$^{E57K/E57K}$, aneurysm; MU-NA, *Fbln4*$^{E57K/E57K}$, nonaneurysm; MU-XA, *Fbln4*$^{E57K/E57K}$;*Lox*$^{+/-}$, extreme aneurysm.

Downloaded from journals.physiology.org/journal/ajpheart at Washington Univ (128.252.014.100) on June 29, 2023.

with WT by 81, 76, and 71%, respectively. These data show increased fragmentation of the elastic laminae in MU ATAs that appear consistent regardless of the aneurysm phenotype.

We also performed en face multiphoton imaging to visualize the IEL density. Representative en face images for each group are shown (Fig. 7*A*) and paired with the respective binary masks (Fig. 7*B*), used for quantification. Although small holes, or fenestrations, are expected in the IEL, MU ATAs have a looser network of elastic fibers that results in some round fenestrations, as well as larger gaps or holes. We quantified the total number of holes (Fig. 7*C*) and the ratio of total hole area to elastin area for the region (Fig. 7*D*). The number of holes is increased in MU-NA, MU-A, and MU-XA ATAs compared with WT by 15.4×, 12.9×, and 17.0×, respectively. There is also a greater ratio of hole to elastin area for MU-NA, MU-A, and MU-XA ATAs compared with WT (107×, 108×, and 110×, respectively). These data show increased holes and decreased overall elastin density of the IEL in the MU ATA regardless of the aneurysm phenotype.

To further investigate extracellular matrix and cellular organization in the ATA wall, we used Movat's pentachrome histological staining (Fig. 8). Consistent with Figs. 5 and 6, MU ATAs have more elastic laminae throughout the wall that are less distinctive, especially toward the adventitia. Collagen is in the adventitia of all ATAs but is interspersed with thin elastin layers in the MU ATAs (particularly in the MU-A and MU-XA samples). Cell layers are present between the medial elastic laminae in all ATAs. MU-XA ATAs have local proteoglycan deposits in the media that were also seen in some MU-A ATAs but were not clearly observed in WT or MU-NA ATAs. The low proteoglycan content overall, small sample size, and high sample variability precluded meaningful quantification of proteoglycan amounts.

Correlations

Correlations between ATA geometry and mass transport parameters (Fig. 9) and ATA geometry, mass transport parameters, and cross-sectional elastic-laminae organization (Fig. 10) were examined. Only data from the MU ATAs were considered to better understand how the genetic mutation and resulting aneurysm phenotype may be related to changes in mass transport and/or elastic-laminae organization. Pearson r values are reported in a correlation matrix containing different metrics of mass transport compared with ATA outer diameters and lengths (Fig. 9*A*). ATA outer diameter is negatively correlated with the three metrics of mass transport (L_p, L_{ps}, and ω, $P \leq 0.0001$–0.001) and positively correlated with axial length ($P < 0.0001$). Length is negatively correlated with L_p and L_{ps} ($P = 0.004$, 0.02), but not ω. Overall, hydraulic conductance correlations are stronger than solute permeability, as shown in the individual plots of hydraulic conductance and solute permeability versus outer diameter (Fig. 9, *B* and *C*). A subset of the complete data set was used to compare geometry, mass transport metrics, and cross-sectional elastic-laminae organization for the MU ATAs. From these data, outer diameter is similarly negatively correlated with mass transport metrics but is only significant for the hydraulic conductance values ($P = 0.02$, 0.003 for L_p and L_{ps}, respectively) (Fig. 10*A*). When we compare elastic-laminae organization to mass transport parameters, end points and slab size are positively correlated with L_p

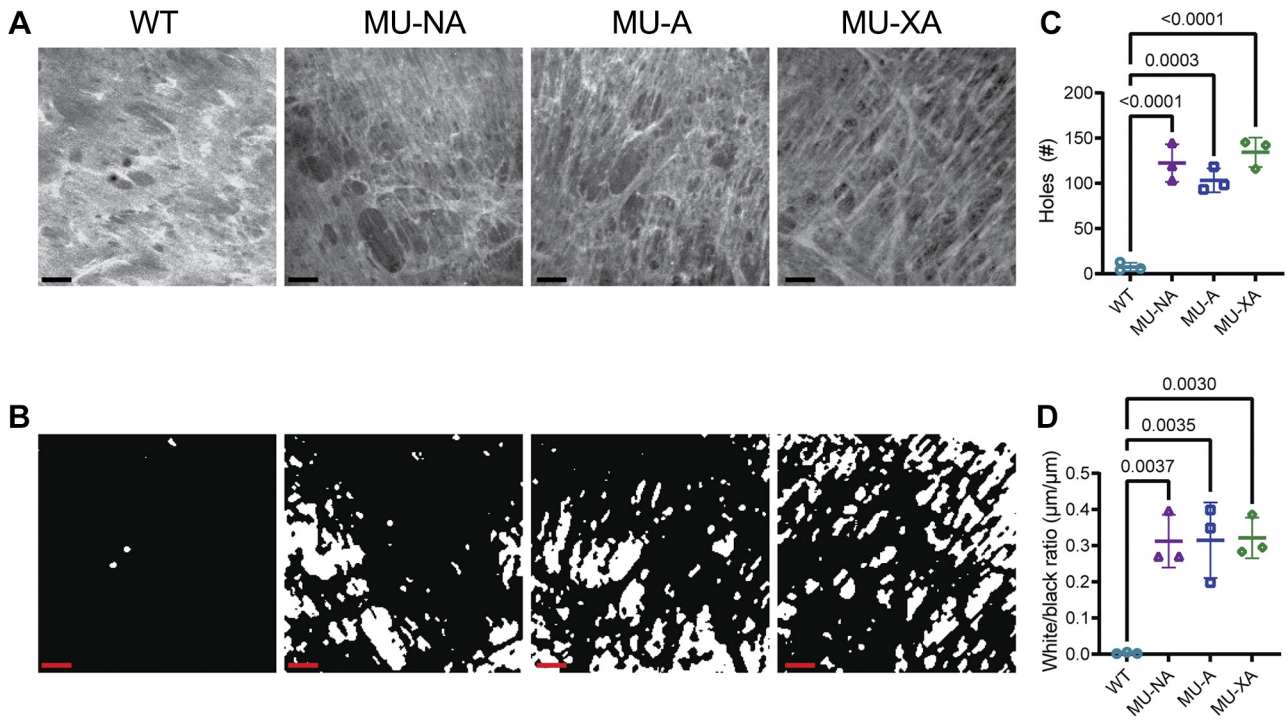

Figure 7. Representative en face multiphoton images of the ascending thoracic aorta (ATA) internal elastic lamina (IEL) (*A*). Associated binary masks are used for quantification of IEL structure (*B*). Fenestrations (+) and larger gaps (*) were all considered holes. Scale bars = 20 μm. The number of holes per image area was quantified and averaged for each ATA (*C*), as were the ratios of white/black pixels (holes/elastin area) from the binary masks (*D*). Significant P values are shown for a one-way ANOVA with Sidak's multiple comparisons. n = 3/group. MU-A, *Fbln4*$^{E57K/E57K}$, aneurysm; MU-NA, *Fbln4*$^{E57K/E57K}$, nonaneurysm; MU-XA, *Fbln4*$^{E57K/E57K}$;*Lox*$^{+/-}$, extreme aneurysm; WT, wild type.

Downloaded from journals.physiology.org/journal/ajpheart at Washington Univ (128.252.014.100) on June 29, 2023.

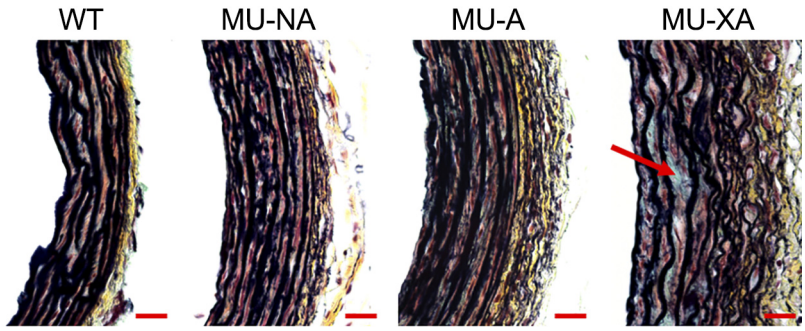

Figure 8. Representative cross-sectional histological images of the ascending thoracic aorta (ATA) from the four experimental groups were stained with Movat's pentachrome that highlights elastic fibers (black), collagen (yellow), cell cytoplasm (red), and proteoglycans (blue). The arrow indicates local proteoglycan deposits in the *Fbln4*$^{E57K/E57K}$;*Lox*$^{+/-}$, extreme aneurysm (MU-XA) ATA. The lumen is on the *left*, and scale bars = 20 μm. Images are representative of *n* = 3/group. MU-A, *Fbln4*$^{E57K/E57K}$, aneurysm; MU-NA, *Fbln4*$^{E57K/E57K}$, nonaneurysm; WT, wild type.

(P = 0.0007, 0.01) and L_{ps} (P = 0.006, 0.01) (Fig. 10, *A* and *B*), and slab size is negatively correlated with diameter and thickness (P = 0.009, 0.012) (Fig. 10*C*). These data show that mass transport parameters correlate with elastic-laminae fragmentation and aneurysm severity, as measured by aortic diameter, and suggest that alterations in mass transport could be linked to aneurysm progression.

DISCUSSION

We measured transmural mass transport in a mouse model of TAA caused by a missense mutation in fibulin-4, which is critical for proper assembly of the aortic extracellular matrix. Using the clinical TAA definition of >50% diameter dilation, we found that the aneurysm phenotype is ~50% penetrant in *Fbln4*$^{E57K/E57K}$ mice, but 100% penetrant if the mice are also heterozygous for lysyl oxidase, an enzyme needed for cross linking of major extracellular matrix components including collagen and elastin. The phenotype variability allowed us to investigate how changes in mass transport and extracellular matrix organization correlate with aneurysm severity, as measured by maximum outer diameter. We speculate how these changes in mass transport may contribute to aneurysm progression or be leveraged for aneurysm treatment.

Mass Transport and Aneurysm Phenotype

Mice with TAA (MU-A and MU-XA) have lower ATA hydraulic conductance and no difference in solute permeability compared with WT. Conversely, mice without TAA (MU-NA) have no difference in ATA hydraulic conductance and higher solute permeability compared with WT. These results suggest that solute permeability may be indicative of early changes in wall structure that precede aneurysm formation, whereas differences in hydraulic conductance occur after or concurrently with aneurysm formation. Our solute is 4-kDa FITC-dextran, chosen because previous modeling efforts suggested that solute flux of small molecules (<70 kDa) was most affected by extracellular matrix organization and elastic-laminae fragmentation in particular (25). Dextran (4 and 70 kDa) probes accumulate in vivo in the thoracic

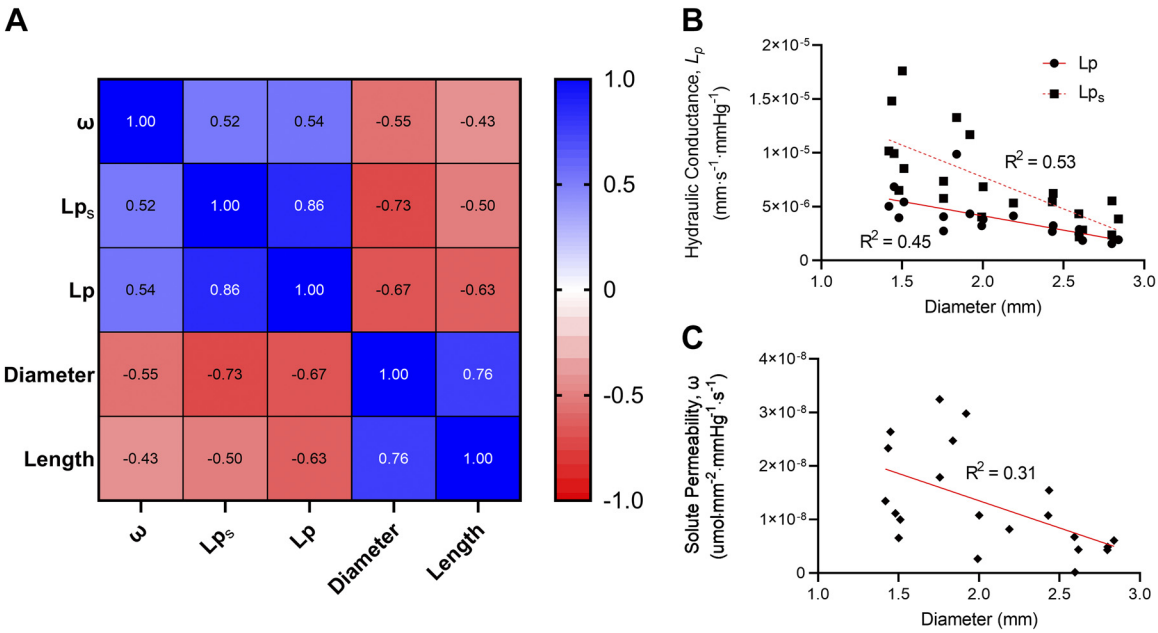

Figure 9. Analyzed relationships of data from *Fbln4*$^{E57K/E57K}$, nonaneurysm (MU-NA), *Fbln4*$^{E57K/E57K}$, aneurysm (MU-A), and *Fbln4*$^{E57K/E57K}$;*Lox*$^{+/-}$, extreme aneurysm (MU-XA) ascending thoracic aortas (ATAs) (n = 21). A full correlation matrix of mass transport metrics, length, and diameter of MU groups (*A*) presented as a heat map to show positive (1.0) and negative (−1.0) Pearson r values. Specific linear correlations of hydraulic conductances vs. diameter (*B*) have R^2 as shown and P = 0.0018, 0.002, for L_p and L_{ps}, respectively. Solute permeability vs. diameter (*C*) has R^2 as shown and P = 0.0093.

Downloaded from journals.physiology.org/journal/ajpheart at Washington Univ (128.252.014.100) on June 29, 2023.

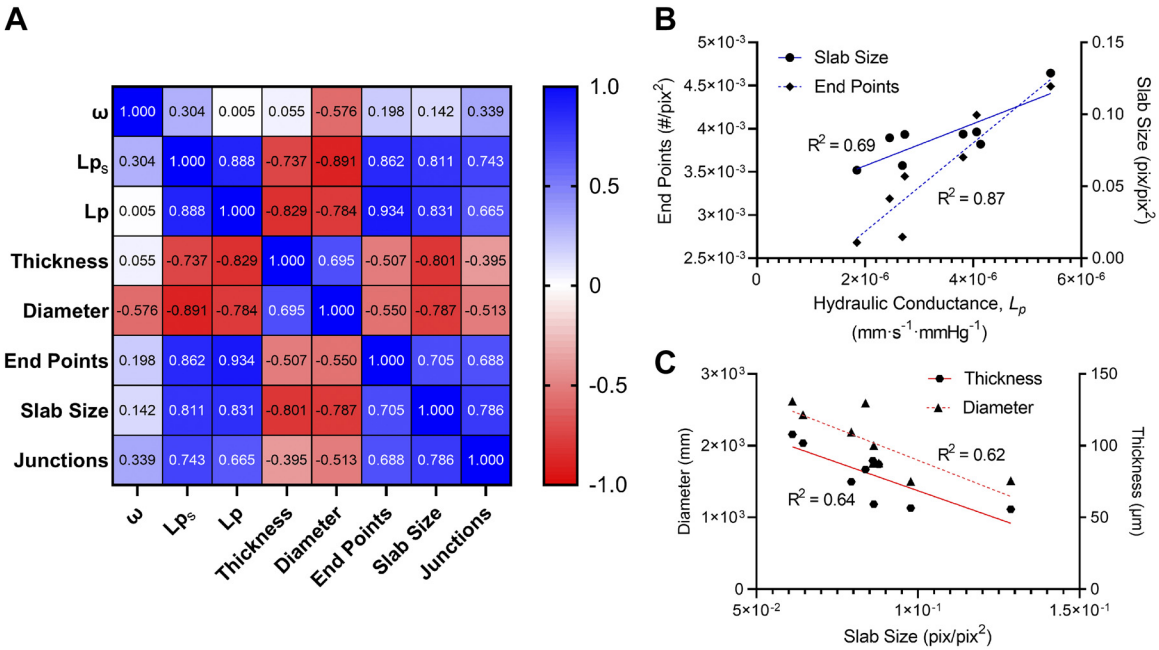

Figure 10. Analyzed relationships of data from *Fbln4*$^{E57K/E57K}$, nonaneurysm (MU-NA), *Fbln4*$^{E57K/E57K}$, aneurysm (MU-A), and *Fbln4*$^{E57K/E57K}$;*Lox*$^{+/-}$, extreme aneurysm (MU-XA) ascending thoracic aortas (ATAs) that had associated cross-sectional images of elastic-laminae structure (n = 8–9). A full correlation matrix of mass transport metrics, thickness, diameter, and elastic-laminae fragmentation metrics with a heat map to show positive (1.0) and negative (−1.0) Pearson r values (*A*). Specific linear correlations of end points and slab size vs. hydraulic conductance (L_p) (*B*) have R^2 as shown and P = 0.0007 and 0.0106, respectively. Diameter and thickness vs. slab size (*C*) have R^2 as shown and P = 0.0119 and 0.0095, respectively.

aorta of a mouse model of TAA caused by treatment with β-aminopropionitrile (BAPN), a lysyl oxidase inhibitor that reduces cross linking of collagen and elastin. Accumulation of the dextran probes at early time points was predictive of aneurysm location (26), suggesting that solute permeability may be an indicator of wall defects leading to aneurysm formation. Small cytokines, such as monocyte chemoattractant protein-1 (12 kDa) and TGF-β (25 kDa), which can play a role in TAA pathogenesis (27), may experience differential transport because of early structural changes in the aortic wall allowing them to act on smooth muscle cells that are typically isolated within a dense extracellular matrix in the medial layer (5). Small molecule pharmaceuticals (<1 kDa) for TAA treatment may be designed to take advantage of the early alterations in solute transport for facilitated delivery to the aortic wall.

Hydraulic conductance, or fluid transport, is reduced in mice with TAA, which could lead to hypoxia within the aortic media and exacerbate aneurysm progression. Cells in the intima and inner media of the aorta are supplied with oxygen from blood flowing through the lumen. In the aorta of large animals, the adventitia and outer media are supplied with oxygen by capillaries in the vasa vasorum. Small animals, such as mice, do not have a vasa vasorum and rely on luminal blood or outer capillaries for oxygen delivery throughout the aortic wall (28). The concentration of oxygen in the mouse aortic wall depends on the oxygen consumption rate and the Sherwood number (29), which is the ratio of convective to diffusive oxygen transfer and will be affected by the hydraulic conductance. Although the adventitia and outer media in humans with TAA would likely not be affected by changes in hydraulic conductance, the inner media would be affected, and there is evidence of medial hypoxia in human TAA (30).

Previously, we investigated transmural mass transport in the ATA of *Lox*$^{M292R/+}$ mice (13), which have fragmented elastic laminae, but no TAA (12), and hence are similar in aneurysm phenotype to our MU-NA mice in the current study. Both *Lox*$^{M292R/+}$ and MU-NA ATA have large, significant increases in solute permeability and no (MU-NA) or slight increases (*Lox*$^{M292R/+}$) in hydraulic conductance (13). These results indicate mass transport changes that correlate with extracellular matrix defects and a tendency toward aneurysm formation with additional stressors, such as lysyl oxidase insufficiency in the current study and increased blood pressure in *Lox*$^{M292R/+}$ mice (14). Hydraulic conductance and solute permeability values for the mouse ATA are comparable between the two studies. Hydraulic conductance values for the mouse ATA are consistent with our previous values for the mouse carotid artery (11) but are an order of magnitude higher than those observed for rabbit (31) and rat (32) aorta and two orders of magnitude higher than that calculated for cells (33). This suggests there are species-specific differences that must be further investigated. This also indicates that solute is likely moving around and not through the cells and highlights the importance of the extracellular matrix for small molecule transport.

Extracellular Matrix Organization

All MU mice (with and without TAA) have increased elastic-laminae fragmentation and decreased elastin density in the IEL, indicating significant extracellular matrix disruption. We hypothesized that extracellular matrix defects would lead

Downloaded from journals.physiology.org/journal/ajpheart at Washington Univ (128.252.014.100) on June 29, 2023.

to mass transport differences that may be linked to aneurysm phenotype. However, the elastic fiber defects appear consistent across groups and do not explain the dependence of mass transport parameters on aneurysm phenotype. We did find hydraulic conductance to positively correlate with elastic-fiber end points and average slab size. The elastic-fiber layers extend into the adventitia in the MU ATAs. Because there is a trend toward an increase in slab size for MU-NA compared with other groups, there may be aberrant formation of additional elastic laminae that later break down and contribute to diameter dilation, which could explain why slab size is negatively correlated with diameter and thickness. Increased numbers of elastic laminae are found in arteries of elastin heterozygous mice (34). Although additional ATAs must be imaged and differences quantified, the electron microscopy images suggest subtle changes in extracellular matrix organization between MU ATA with 50% aneurysm penetrance and MU-XA ATA with 100% aneurysm penetrance that may cause molecular level changes in mass transport resulting in the observed differences in hydraulic conductance and solute permeability for mice with and without TAA. These data demonstrate possible linkages between extracellular matrix remodeling, mass transport, and diameter dilation.

Although limited samples were examined, medial proteoglycan deposits were observed more often in MU-XA and MU-A ATAs than in MU-NA and WT ATAs. Proteoglycan deposits appear in areas of disrupted elastic laminae in human TAA (6). There is accumulation of the large aggregating proteoglycans aggrecan and versican in human and mouse TAA (7). Loss of function mutations in the small leucine-rich proteoglycan biglycan have been linked to TAA, but its functional role in the disease is still being investigated (35). Proteoglycans are proteins with covalently attached chains of glycosaminoglycans that are highly negatively charged, allowing them to sequester water and solutes (36). Hydraulic conductivity, or the hydraulic conductance normalized for the microscopic path length, is inversely related to glycosaminoglycan concentration in a tissue (37). Increased proteoglycan content could lead to increased fluid sequestration and decreased hydraulic conductance, as observed in the MU-XA and MU-A ATAs. Increased fluid sequestration by proteoglycans is postulated to lead to stress concentrations and swelling pressures between elastic laminae that contribute to TAA dissection (38).

Increased elastic-laminae fragmentation and decreased elastin density in the IEL suggest there may be less resistance to fluid and solute transport through the aortic wall. This is what we observed in our previous studies with genetically modified mice using carotid arteries (11) and ATA (13) with elastic-laminae fragmentation but no diameter dilation. This is also what we observe in the MU-NA ATA in the current study. However, despite fragmented elastic laminae and larger/more holes in the IEL, solute permeability is similar to and hydraulic conductance is decreased in MU-A and MU-XA ATA compared with WT. Like the decreased hydraulic conductance, the similar solute permeability despite the lack of intact elastic laminae may be related to the proteoglycan content of the wall. The 4-kDa FITC-dextran molecule is minimally charged, but its movement may still be retarded by the presence of negatively charged proteoglycans in the wall. Aggrecan concentration negatively correlates with local diffusivity of a 150-kDa antibody in cartilage samples, suggesting that it acts as a barrier to macromolecular transport (39). Although the solute permeability is unchanged in MU-A and MU-XA ATA compared with WT, solute uptake (not measured) may be increased as solute passes through the sparse elastin network and then is retained by proteoglycan pools.

Mass Transport and TAA Pathology

Genetic mutations causing TAA have been linked to the elastin-smooth muscle cell contractile unit [which includes elastic fibers, smooth muscle cell contractile machinery, focal adhesions, nuclear positioning, and other extracellular matrix (ECM) components] and the TGF-β signaling pathway (3). Regardless of the initial genetic mutation, aneurysm progression is influenced by a host of intrinsic and extrinsic factors, of which fluid and solute transport across and within the aortic wall may be a contributor. TAA severity, and hence the guideline for surgical treatment, is currently determined by the aortic diameter or diameter growth rate. We show that ATA diameter in MU mice with a genetic mutation causing TAA susceptibility negatively correlates with solute permeability and hydraulic conductance. For hydraulic conductance, values start near WT and then decrease with aneurysm severity. For solute permeability, values start above WT and then decrease back toward WT with aneurysm severity. The trends suggest that variations in mass transport properties may contribute to the progression of, be used to determine severity of, and/or be leveraged for treatment of TAA.

Limitations

We used a genetic mouse model of TAA (15) that has inherent limitations. The mouse ATA has less elastic laminae (8–10) than human (55–60) (40) and has no vasa vasorum, which may lead to differences in mass transport properties. Despite these differences, the changes in extracellular matrix organization in the MU ATA are consistent with those observed in human TAA and may help explain the associated changes in mass transport and aneurysm severity. Because of the small size of the mouse ATA, our mass transport experiments do not have sufficient resolution to directly calculate the reflection coefficients. We assume that the reflection coefficients are constant and unaffected by the extracellular matrix changes, which must be confirmed in future work. In the current study, we assume 1-D, homogeneous mass transport. Future experimental and/or computational work is needed to investigate the influence of multidirectional and/or localized mass transport in TAA, which may involve more detailed tracking of fluid and solute movement. Because of the experimental design, we had a smaller number of samples for quantification of the extracellular matrix organization than for the mass transport properties, and so correlations were not possible on the full data set. Movat's pentachrome staining that highlighted local proteoglycan deposits was performed on a limited number of samples. Further investigation is needed to determine the role of specific proteoglycans (i.e., aggrecan, biglycan) in transmural mass transport and TAA.

Conclusions

To our knowledge, this is the first report of ATA transmural mass transport properties, hydraulic conductance,

Downloaded from journals.physiology.org/journal/ajpheart at Washington Univ (128.252.014.100) on June 29, 2023.

and solute permeability for a mouse model with clinically defined TAA of >50% diameter dilation. We show an increase in solute permeability for the MU-NA ATA with no TAA, despite measurable elastic-laminae fragmentation and a decrease in hydraulic conductance for MU-A and MU-XA ATAs with TAA, measurable elastic-laminae fragmentation, and observed proteoglycan deposits. Our results show that elastic-laminae fragmentation is associated with an increase in solute permeability of the aortic wall that precedes aneurysm formation. Following aneurysm formation, the aortic wall has decreased hydraulic conductance that may be related to water sequestration by proteoglycans that could alter transmural oxygen concentrations. The reported transport properties can be used in computational models for a more sophisticated understanding of aortic wall mass transport behavior in TAA. Overall, our results suggest relationships between extracellular matrix organization, mass transport properties, and TAA severity, as measured by maximum diameter, which may be used to guide future studies for TAA prevention and/or treatment.

DATA AVAILABILITY

All data are included in the published article.

GRANTS

This study was partially funded by American Heart Association Grant 19TPA-34910047 and National Heart, Lung, and Blood Institute Grants R01HL164800 and K08HL135400.

DISCLOSURES

No conflicts of interest, financial or otherwise, are declared by the authors.

AUTHOR CONTRIBUTIONS

C.L.C., C.M.H., and J.E.W. conceived and designed research; C.L.C., K.A.K., and C.M.H. performed experiments; C.L.C., Y.W., K.A.K., M.R.B., and J.E.W. analyzed data; C.L.C., Y.W., M.R.B., C.M.H., and J.E.W. interpreted results of experiments; C.L.C., Y.W., C.M.H., and J.E.W. prepared figures; C.L.C. and J.E.W. drafted manuscript; C.L.C., K.A.K., M.R.B., C.M.H., and J.E.W. edited and revised manuscript; C.L.C., Y.W., K.A.K., M.R.B., C.M.H., and J.E.W. approved final version of manuscript.

REFERENCES

1. **Johnston KW**, **Rutherford RB**, **Tilson MD**, **Shah DM**, **Hollier L**, **Stanley JC.** Suggested standards for reporting on arterial aneurysms. Subcommittee on Reporting Standards for Arterial Aneurysms, Ad Hoc Committee on Reporting Standards, Society for Vascular Surgery and North American Chapter, International Society for Cardiovascular Surgery. *J Vasc Surg* 13: 452–458, 1991. doi:10.1067/mva.1991.26737.
2. **Elefteriades JA**, **Sang A**, **Kuzmik G**, **Hornick M.** Guilt by association: paradigm for detecting a silent killer (thoracic aortic aneurysm). *Open Heart* 2: e000169, 2015. doi:10.1136/openhrt-2014-000169.
3. **Rodrigues Bento J**, **Meester J**, **Luyckx I**, **Peeters S**, **Verstraeten A**, **Loeys B.** The genetics and typical traits of thoracic aortic aneurysm and dissection. *Annu Rev Genomics Hum Genet* 23: 223–253, 2022. doi:10.1146/annurev-genom-111521-104455.
4. **Dal Canto AJ**, **Swanson PE**, **O'Guin AK**, **Speck SH**, **Virgin HW.** IFN-γ action in the media of the great elastic arteries, a novel immunoprivileged site. *J Clin Invest* 107: R15–R22, 2001. doi:10.1172/JCI11540.
5. **Michel JB**, **Thaunat O**, **Houard X**, **Meilhac O**, **Caligiuri G**, **Nicoletti A.** Topological determinants and consequences of adventitial responses to arterial wall injury. *Arterioscler Thromb Vasc Biol* 27: 1259–1268, 2007. doi:10.1161/ATVBAHA.106.137851.
6. **Pomerance A**, **Yacoub MH**, **Gula G.** The surgical pathology of thoracic aortic aneurysms. *Histopathology* 1: 257–276, 1977. doi:10.1111/j.1365-2559.1977.tb01665.x.
7. **Cikach FS**, **Koch CD**, **Mead TJ**, **Galatioto J**, **Willard BB**, **Emerton KB**, **Eagleton MJ**, **Blackstone EH**, **Ramirez F**, **Roselli EE**, **Apte SS.** Massive aggrecan and versican accumulation in thoracic aortic aneurysm and dissection. *JCI Insight* 3: e97167, 2018. doi:10.1172/jci.insight.97167.
8. **Mieremet A**, **van der Stoel M**, **Li S**, **Coskun E**, **van Krimpen T**, **Huveneers S**, **de Waard V.** Endothelial dysfunction in Marfan syndrome mice is restored by resveratrol. *Sci Rep* 12: 22504, 2022. doi:10.1038/s41598-022-26662-5.
9. **Tada S**, **Tarbell JM.** Fenestral pore size in the internal elastic lamina affects transmural flow distribution in the artery wall. *Ann Biomed Eng* 29: 456–466, 2001. doi:10.1114/1.1376410.
10. **López-Guimet J**, **Andilla J**, **Loza-Alvarez P**, **Egea G.** High-resolution morphological approach to analyse elastic laminae injuries of the ascending aorta in a murine model of Marfan syndrome. *Sci Rep* 7: 1505, 2017. doi:10.1038/s41598-017-01620-8.
11. **Cocciolone AJ**, **Johnson E**, **Shao JY**, **Wagenseil JE.** Elastic fiber fragmentation increases transmural hydraulic conductance and solute transport in mouse arteries. *J Biomech Eng* 141: 021013, 2019. doi:10.1115/1.4042173.
12. **Lee Vivian S**, **Halabi Carmen M**, **Hoffman Erin P**, **Carmichael N**, **Leshchiner I**, **Lian CG**, **Bierhals AJ**, **Vuzman D**, **Brigham Genomic Medicine**, **Mecham RP**, **Frank NY**, **Stitziel NO.** Loss of function mutation in LOX causes thoracic aortic aneurysm and dissection in humans. *Proc Natl Acad Sci USA* 113: 8759–8764, 2016. doi:10.1073/pnas.1601442113.
13. **Crandall CL**, **Kim SY**, **Rother J**, **Lee VS**, **Mecham RP**, **Wagenseil JE.** Increases in hydraulic conductance and solute permeability in a mouse model of ascending thoracic aortic aneurysm. *J Biomech* 145: 111360, 2022. doi:10.1016/j.jbiomech.2022.111360.
14. **Lee VS**, **Halabi CM**, **Broekelmann TJ**, **Trackman PC**, **Stitziel NO**, **Mecham RP.** Intracellular retention of mutant lysyl oxidase leads to aortic dilation in response to increased hemodynamic stress. *JCI Insight* 4: e127748, 2019. doi:10.1172/jci.insight.127748.
15. **Igoucheva O**, **Alexeev V**, **Halabi CM**, **Adams SM**, **Stoilov I**, **Sasaki T**, **Arita M**, **Donahue A**, **Mecham RP**, **Birk DE**, **Chu ML.** Fibulin-4 E57K knock-in mice recapitulate cutaneous, vascular and skeletal defects of recessive cutis laxa 1b with both elastic fiber and collagen fibril abnormalities. *J Biol Chem* 290: 21443–21459, 2015. doi:10.1074/jbc.M115.640425.
16. **McLaughlin PJ**, **Chen Q**, **Horiguchi M**, **Starcher BC**, **Stanton JB**, **Broekelmann TJ**, **Marmorstein AD**, **McKay B**, **Mecham R**, **Nakamura T**, **Marmorstein LY.** Targeted disruption of fibulin-4 abolishes elastogenesis and causes perinatal lethality in mice. *Mol Cell Biol* 26: 1700–1709, 2006. doi:10.1128/MCB.26.5.1700-1709.2006.
17. **Noda K**, **Kitagawa K**, **Miki T**, **Horiguchi M**, **Akama TO**, **Taniguchi T**, **Taniguchi H**, **Takahashi K**, **Ogra Y**, **Mecham RP**, **Terajima M**, **Yamauchi M**, **Nakamura T.** A matricellular protein fibulin-4 is essential for the activation of lysyl oxidase. *Sci Adv* 6: eabc1404, 2020. doi:10.1126/sciadv.abc1404.
18. **Halabi CM**, **Broekelmann TJ**, **Lin M**, **Lee VS**, **Chu ML**, **Mecham RP.** Fibulin-4 is essential for maintaining arterial wall integrity in conduit but not muscular arteries. *Sci Adv* 3: e1602532, 2017. doi:10.1126/sciadv.1602532.
19. **Hornstra IK**, **Birge S**, **Starcher B**, **Bailey AJ**, **Mecham RP**, **Shapiro SD.** Lysyl oxidase is required for vascular and diaphragmatic development in mice. *J Biol Chem* 278: 14387–14393, 2003. doi:10.1074/jbc.M210144200.
20. **Wagenseil JE**, **Nerurkar NL**, **Knutsen RH**, **Okamoto RJ**, **Li DY**, **Mecham RP.** Effects of elastin haploinsufficiency on the mechanical behavior of mouse arteries. *Am J Physiol Heart Circ Physiol* 289: H1209–H1217, 2005. doi:10.1152/ajpheart.00046.2005.
21. **Kedem O**, **Katchalsky A.** Thermodynamic analysis of the permeability of biological membranes to non-electrolytes. *Biochim Biophys Acta* 27: 229–246, 1958. doi:10.1016/0006-3002(58)90330-5.
22. **Cussler EL.** *Diffusion: Mass Transfer in Fluid Systems*. Cambridge, UK: Cambridge University Press, 2009.

Downloaded from journals.physiology.org/journal/ajpheart at Washington Univ (128.252.014.100) on June 29, 2023.

23. **Karmakar N**, **Lever MJ.** Effects of high molecular weight solutes on fluid flux across the arterial wall. *Heart Vessels* 9: 275–282, 1994. doi:10.1007/BF01745092.
24. **Arganda-Carreras I**, **Fernández-González R**, **Muñoz-Barrutia A**, **Ortiz-De-Solorzano C.** 3D reconstruction of histological sections: application to mammary gland tissue. *Microsc Res Tech* 73: 1019–1029, 2010. doi:10.1002/jemt.20829.
25. **Guang Y**, **Cocciolone AJ**, **Crandall CL**, **Johnston BB**, **Setton LA**, **Wagenseil JE.** A multiphasic model for determination of water and solute transport across the arterial wall: effects of elastic fiber defects. *Arch Appl Mech* 92: 447–459, 2022. doi:10.1007/s00419-021-01985-3.
26. **Yang X**, **Xu C**, **Yao F**, **Ding Q**, **Liu H**, **Luo C**, **Wang D**, **Huang J**, **Li Z**, **Shen Y**, **Yang W**, **Li Z**, **Yu F**, **Fu Y**, **Wang L**, **Ma Q**, **Zhu J**, **Xu F**, **Cong X**, **Kong W.** Targeting endothelial tight junctions to predict and protect thoracic aortic aneurysm and dissection. *Eur Heart J* 44: 1248–1261, 2023. doi:10.1093/eurheartj/ehac823.
27. **Pisano C**, **Balistreri CR**, **Ricasoli A**, **Ruvolo G.** Cardiovascular disease in ageing: an overview on thoracic aortic aneurysm as an emerging inflammatory disease. *Mediators Inflamm* 2017: 1274034, 2017. doi:10.1155/2017/1274034.
28. **Wolinsky H**, **Glagov S.** Nature of species differences in the medial distribution of aortic vasa vasorum in mammals. *Circ Res* 20: 409–421, 1967. doi:10.1161/01.res.20.4.409.
29. **Tarbell J**, **Mahmoud M**, **Corti A**, **Cardoso L**, **Caro C.** The role of oxygen transport in atherosclerosis and vascular disease. *J R Soc Interface* 17: 20190732, 2020. doi:10.1098/rsif.2019.0732.
30. **Billaud M**, **Hill JC**, **Richards TD**, **Gleason TG**, **Phillippi JA.** Medial hypoxia and adventitial vasa vasorum remodeling in human ascending aortic aneurysm. *Front Cardiovasc Med* 5: 124, 2018. doi:10.3389/fcvm.2018.00124.
31. **Tedgui A**, **Lever MJ.** Filtration through damaged and undamaged rabbit thoracic aorta. *Am J Physiol* 247: H784–791, 1984. doi:10.1152/ajpheart.1984.247.5.H784.
32. **Shou Y**, **Jan KM**, **Rumschitzki DS.** Transport in rat vessel walls. I. Hydraulic conductivities of the aorta, pulmonary artery, and inferior vena cava with intact and denuded endothelia. *Am J Physiol Heart Circ Physiol* 291: H2758–H2771, 2006. doi:10.1152/ajpheart.00610.2005.
33. **He Y**, **Devireddy RV.** An inverse approach to determine solute and solvent permeability parameters in artificial tissues. *Ann Biomed Eng* 33: 709–718, 2005. doi:10.1007/s10439-005-1511-x.
34. **Faury G**, **Pezet M**, **Knutsen RH**, **Boyle WA**, **Heximer SP**, **McLean SE**, **Minkes RK**, **Blumer KJ**, **Kovacs A**, **Kelly DP**, **Li DY**, **Starcher B**, **Mecham RP.** Developmental adaptation of the mouse cardiovascular system to elastin haploinsufficiency. *J Clin Invest* 112: 1419–1428, 2003. doi:10.1172/JCI19028.
35. **Meester JAN**, **De Kinderen P**, **Verstraeten A**, **Loeys BL.** The role of biglycan in the healthy and thoracic aneurysmal aorta. *Am J Physiol Cell Physiol* 322: C1214–C1222, 2022. doi:10.1152/ajpcell.00036.2022.
36. **Jana S**, **Hu M**, **Shen M**, **Kassiri Z.** Extracellular matrix, regional heterogeneity of the aorta, and aortic aneurysm. *Exp Mol Med* 51: 1–15, 2019. doi:10.1038/s12276-019-0286-3.
37. **Levick JR.** Flow through interstitium and other fibrous matrices. *Q J Exp Physiol* 72: 409–437, 1987. doi:10.1113/expphysiol.1987.sp003085.
38. **Roccabianca S**, **Ateshian GA**, **Humphrey JD.** Biomechanical roles of medial pooling of glycosaminoglycans in thoracic aortic dissection. *Biomech Model Mechanobiol* 13: 13–25, 2014. doi:10.1007/s10237-013-0482-3.
39. **DiDomenico CD**, **Kaghazchi A**, **Bonassar LJ.** Measurement of local diffusion and composition in degraded articular cartilage reveals the unique role of surface structure in controlling macromolecular transport. *J Biomech* 82: 38–45, 2019. doi:10.1016/j.jbiomech.2018.10.019.
40. **Wolinsky H**, **Glagov S.** A lamellar unit of aortic medial structure and function in mammals. *Circ Res* 20: 99–111, 1967. doi:10.1161/01.res.20.1.99.

Downloaded from journals.physiology.org/journal/ajpheart at Washington Univ (128.252.014.100) on June 29, 2023.